Journal of Materials Science: Materials in Electronics (2020) 31:2862–2876
https://doi.org/10.1007/s10854-019-02831-7

Investigation on shear fracture of different strain rates for Cu/Cu_3Sn/Cu solder joints derived from Cu–15μm Sn–Cu sandwich structure

Peng Yao[1] · Xiaoyan Li[1]

Received: 2 November 2019 / Accepted: 26 December 2019 / Published online: 8 January 2020
© Springer Science+Business Media, LLC, part of Springer Nature 2020

Abstract

Full intermetallics (IMCs) solder joints are of great significance to electronic packaging technology. In this paper, some efforts have been made for bridging research gap on reliabilities of such joints. Shear fracture of different strain rates, for Cu/Cu_3Sn/Cu joints derived from Cu–15μm Sn–Cu sandwich structure, was comprehensively analyzed. With the strain rates of 6.67×10^{-2} s^{-1}, 6.67×10^{-1} s^{-1} , and 6.67 s^{-1}, the shear strength of Cu/Cu_3Sn/Cu joints was, respectively, 44 MPa, 48.4 MPa, and 57.6 MPa, which presented an ascending trend. The increased strength of joints was attributed to the intensification of work-hardening effect within interfacial region. For the strain rates of 6.67×10^{-2} s^{-1} and 6.67×10^{-1} s^{-1}, the fracture of joints was both a mixture of transgranular fracture and intergranular fracture within Cu_3Sn, while the fractured path both had no diversion and kept continuous. For the strain rate of 6.67 s^{-1}, only transgranular fracture occurred within Cu_3Sn, and the fractured path diverted with the appearance of step. The transgranular fracture at these three strain rates all belonged to cleavage fracture, and their proportion presented the increasing trend of 25.5% → 59.5% → 100% (Strain rates: 6.67×10^{-2} s^{-1} → 6.67×10^{-1} s^{-1} → 6.67 s^{-1}). Because of the fracture mechanism of different strain rates, the crack propagation resistance increased by a larger extent for 6.67×10^{-1} s^{-1} → 6.67 s^{-1} in comparison with that for 6.67×10^{-2} s^{-1} → 6.67×10^{-1} s^{-1}. Moreover, the strain rate sensitivity of Cu/Cu_3Sn/Cu joints was smaller than that of conventional joints, which was due to the different interfacial structure of two joints.

1 Introduction

With the coming of Artificial Intelligence (AI) and Internet of Things (IOT) era, the chips industry has obtained an increasing number of attentions because of its significant effects on AI and IOT [1–4]. As one part of the whole industry chain of chips, electronic packaging technology plays quite an important role, because it is the precondition for chips realizing anticipated functions. Specifically, electronic packaging technology refers to placing chips on frames or substrates for arrangement and fixation firstly [5, 6]. Then, chips are encapsulated through pouring special materials for protection and support, which is followed by mounting the encapsulated chips on Print Circuit Boards (PCBs). Finally, the system or structure with certain functions is installed.

For the electronic packaging, interconnected technology is a key element because of its bridging effect among chips, frames and PCBs [7]. The interconnected technology includes several methods, such as wire bonding, flip chip, and so on.[8]. Essentially, most of these methods are realized through soldering process, because the soldering process has advantage of high cost performance and little damage on chips. When the soldering process is ended, solder joints obtained mainly play functions in following aspects [9]. On the one hand, they provide thermal and electrical conduction to the connected devices. On the other hand, they also give mechanical support to the connected devices. Thus, the quality of solder joints is bound to affect the quality of electronic packaging, which means it is of great importance to conduct studies regarding solder joints within electronic packaging.

Generally, solder thickness for soldering process within electronic packaging is several hundreds of micrometers. The solder thickness is also called the interconnected height. Under such interconnected height, the solder cannot be consumed completely during soldering process, which means

✉ Peng Yao
kaka3778@126.com

✉ Xiaoyan Li
xyli@bjut.edu.cn

[1] College of Materials Science and Engineering, Beijing University of Technology, No.100 Ping Le Yuan, Chaoyang District, Beijing 100124, China

the joints obtained (hereafter mentioned as conventional joints) have the interfacial structure of substrates/IMCs/solder/IMCs/substrates [10–16]. The residual solder takes up quite a large proportion in comparison with interfacial IMCs for conventional joints. As there is a trend for consumer electronics having multifunctionality and portability in recent years, several changes have been made to comply with the trend in some electronic products. For example, more and more function modules are mounted within these electronic products, and the volume of these electronic products is declined. As a result, the interconnected height is declined from several hundreds of micrometers to less than dozens of micrometers. With the decreased interconnected height, the solder can be consumed completely to produce IMCs if soldering time is extended suitably [17–21]. This indicates full IMCs joints, with the interfacial structure of substrates/IMCs/substrates, can be obtained under the declined interconnected height. It is clearly seen that full IMCs joints have the interfacial structure different from that of conventional joints. Due to high melting point of IMCs, full IMCs joints can service under high temperature, indicating they have great significance to electronic packaging.

By now, the studies related to solder joints of electronic packaging have mainly focused on conventional joints. Because of the difference in interconnected height, there must be difference regarding soldering process between full IMCs joints and conventional joints [10, 11, 17, 18]. Then, the difference in soldering process causes difference of interfacial structure for the two joints [12–14, 19–21], while the different interfacial structure further leads to difference in reliabilities of the two joints [15, 16, 19–21]. In other words, the study findings for conventional joints, which involve the soldering process, interfacial phase evolution, and reliabilities, cannot shed adequate guidance on corresponding studies of full IMCs joints. Thus, it is necessary to study these aspects of full IMCs joints.

For the quality of full IMCs joints, the reliabilities of joints play quite an important indicator. Unfortunately, the studies paid attention to reliabilities of such joints are not adequate. The existed studies only focus on the reliabilities under a specific service condition [19–21], while no study focuses on the reliabilities under different service conditions. Some endeavors have been done in this paper for bridging the research gap. As a matter of fact, solder joints within electronic products confront varied strain rates during the use of electronic products [22]. Because there is mismatch of thermal expansion coefficient between solder and substrates, thermal stress is produced, resulting in strain rates of low level. Comparatively, mechanical vibrations of electronic products lead to moderate strain rates, while strain rates of a high level are caused with accidental drops of electronic products. For the common Cu–Sn soldering system within electronic packaging, it is known Sn solder can be totally consumed to form Cu/Cu_3Sn/Cu joints as the interconnected height less than dozens of micrometers [17, 18]. When the reliabilities of joints are evaluated in electronics industry, shear test actually acts as a main method. Therefore, based on the above, Cu/Cu_3Sn/Cu solder joints were primarily fabricated from Cu–15μm Sn–Cu sandwich structure in this paper, and the shear fracture of Cu/Cu_3Sn/Cu joints under different strain rates was further studied.

2 Experimental details

2.1 Fabrication of Cu/Cu_3Sn/Cu joints

In order to fabricate Cu/Cu_3Sn/Cu solder joints, pure Sn was used as solder, while high pure polycrystalline Cu foils, with the size of 2 mm × 2 mm × 1 mm, were used as substrates. The Sn solder was electroplated on Cu surface with the area of 2 mm × 2 mm. The thickness of each Sn layer on the Cu surface was controlled to be 7.5 μm. For electroplating Sn solder, the flatness of Cu surface is quite important. Therefore, several measures were done to ensure the flatness of Cu surface. At first, abrasive papers (#800, #1000, #1500, #2000 and #3000) were adopted to grind the Cu surface. Then, the Cu surface was mechanically polished using diamond polishing paste with the grain diameter of 0.5 μm. After the electroplating of Sn solder was finished, the Sn solder was cleaned and dried successively. Next, two Cu substrates with Sn layers of 7.5 μm were aligned through a special clamp. As a result, Cu–15μm Sn–Cu sandwich structure was formed, which indicated the interconnected height during soldering was 15 μm. Figure 1 presents the schematic illustration for forming Cu–15μm Sn–Cu sandwich structure.

After the Cu–15μm Sn–Cu sandwich structure was obtained, soldering process was conducted on the Cu–15μm Sn–Cu sandwich structure using tube furnaces. During the soldering process, the tube furnace was full of pure Ar as protection gas. The formation of Cu/Cu_3Sn/Cu joints means that Sn solder is totally consumed and transformed into Cu_3Sn. As a result, it is necessary to control soldering process parameters for guaranteeing the formation of Cu/Cu_3Sn/Cu joints. Specifically, the soldering temperature, soldering pressure, and soldering time were controlled to be 260 °C, 0.04 MPa, and 40 h. It should be noted that the soldering pressure of 0.04 MPa was applied along the thickness direction of Sn solder. Because the fabrication of Cu/Cu_3Sn/Cu joints was realized under the small interconnected height of 15 μm, the application of pressure was very important. It was thought that applying soldering pressure could make the Cu–15μm Sn–Cu sandwich structure contact tightly, which was good for improving the capillarity of liquid Sn on Cu substrates during soldering. Since the solder capillarity

was improved, the quality of joints could be ensured. The schematic illustration, which describes the application of pressure on Cu–15μm Sn–Cu sandwich structure, is presented in Fig. 2. With the finish of soldering process, all the obtained joints were taken out from tube furnaces and cooled in ambient environment.

2.2 Shear test of Cu/Cu_3Sn/Cu joints

Shear test was conducted on Cu/Cu_3Sn/Cu joints using one uniaxial microforce test system. Moreover, the shear test was carried out at room temperature, and a special clamp was used to fix the joints during the shear test. Figure 3 gives the schematic illustration of shear test. The joints were sheared under different strain rates which were 6.67×10^{-2} s^{-1}, 6.67×10^{-1} s^{-1}, and 6.67 s^{-1}, respectively. After that, the

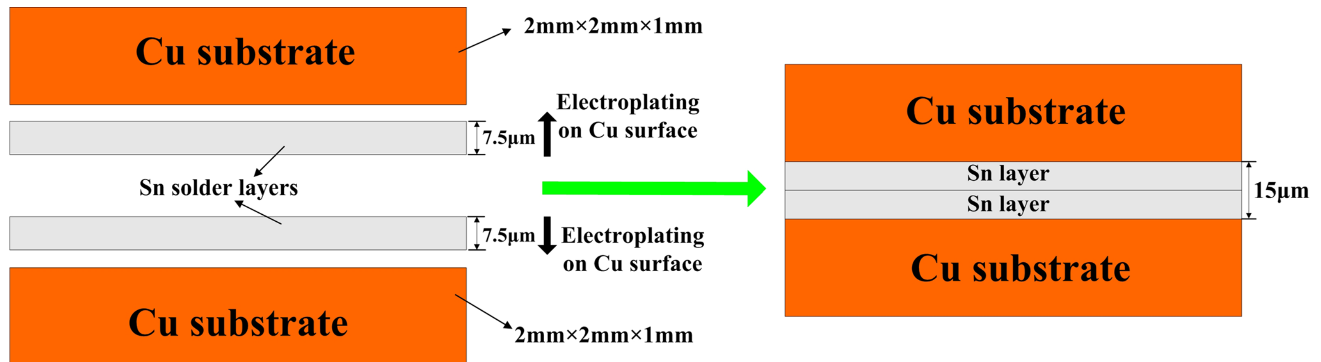

Fig. 1 Schematic illustration for the formation of Cu–15μm Sn–Cu sandwich structure

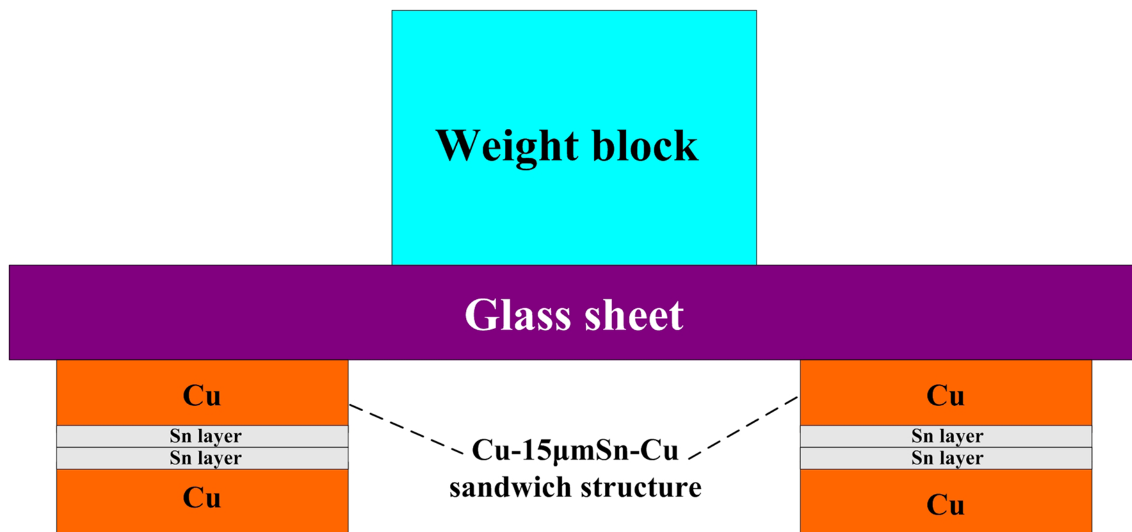

Fig. 2 Schematic illustration for the application of pressure on Cu–15μm Sn–Cu sandwich structure

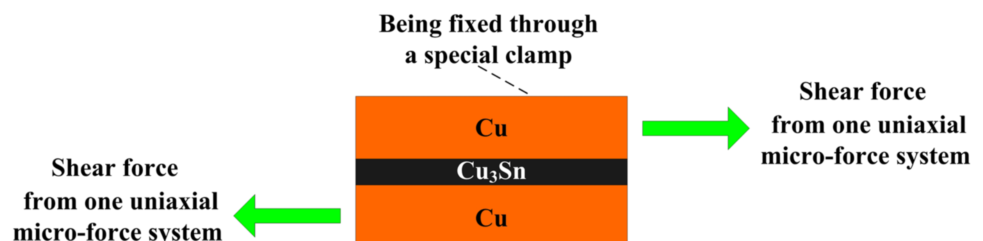

Fig. 3 Schematic illustration of shear test for Cu/Cu_3Sn/Cu joints

mathematic average of shear strength of joints was calculated for each strain rate. It should be noted that the different strain rates were obtained through different loading rates of shear test.

2.3 Characterization and fracture analysis of $Cu/Cu_3Sn/Cu$ joints

In order to observe connected status and verify interfacial microstructure, interfacial region of $Cu/Cu_3Sn/Cu$ joints needed to be characterized. The interfacial region of joints actually refers to the area between Cu substrates of opposite sides. Figure 4 presents the schematic illustration of interfacial region for $Cu/Cu_3Sn/Cu$ joints. For the characterization, metallographic cross-sections of joints were prepared. The following method was used to prepare the metallographic cross-sections. The method successively included the mount of joints in epoxy resin, grind using abrasive papers (#800, #1000, #1500, #2000, #3000) and mechanical polishing using diamond polishing paste (0.5 μm). After the preparation of metallographic cross-sections, the interfacial region was, respectively, characterized by optical microscope (OM), scanning electron microscope (SEM) under backscattered electron signal, as well as X-ray diffraction (XRD). The OM images were used to analyze the connected status, while the SEM images, as well as the XRD result, were used to confirm the interfacial microstructure. It should be noted that the 2θ was changed from 25° to 80° for XRD.

After the shear test, cross-sectional fractured morphologies of $Cu/Cu_3Sn/Cu$ joints were observed by SEM with backscattered electron signal, while top-view fractured morphologies of joints were observed by SEM with secondary electron signal. For observing the cross-sectional fractured morphologies, the sheared joints also experienced the above method for preparing metallographic cross-sections. For the top-view fractured morphologies of each strain rate, SEM images of different positions were taken. Within each SEM image, the area of different fracture was, respectively, measured using Image J software. As a result, the area proportion of different fracture in each image was obtained. For each strain rate, the area proportion of different images was averaged. The obtained mathematic average of one strain rate was finally regarded as the proportion of corresponding fracture under the strain rate.

3 Results and discussion

3.1 Shear strength of $Cu/Cu_3Sn/Cu$ joints under different strain rates

Figure 5 shows the interfacial region of joints after soldering the Cu–15μm Sn–Cu sandwich structure at 260 °C, 0.04 MPa, and 40 h. Figure 6 shows the XRD pattern for the interfacial region of joints. As shown in Figs. 5 and 6, after the Cu–15μm Sn–Cu sandwich structure was soldered at 260 °C, 0.04 MPa, and 40 h, Sn solder was completely

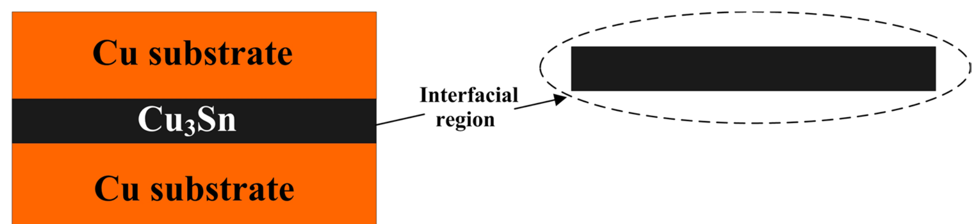

Fig. 4 Schematic illustration of interfacial region for $Cu/Cu_3Sn/Cu$ joints

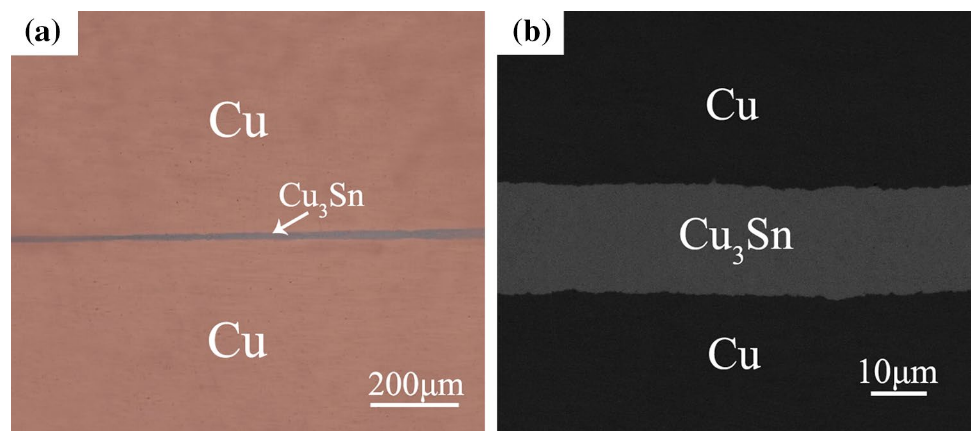

Fig. 5 Interfacial region of joints after soldering of Cu–15μm Sn–Cu sandwich structure (260 °C, 0.04 MPa, 40 h). **a** OM image **b** SEM image

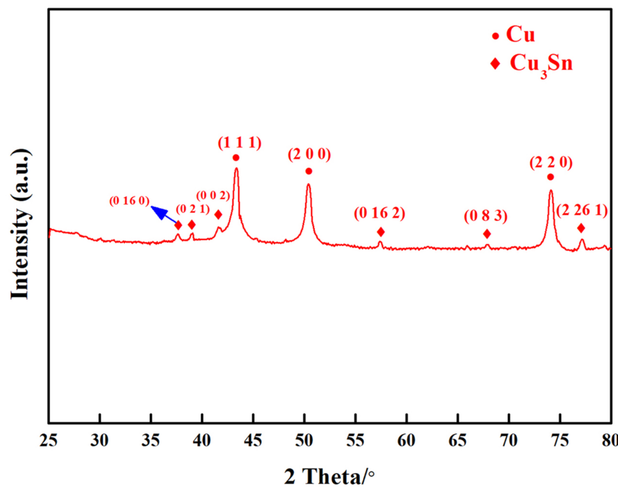

Fig. 6 XRD pattern for the interfacial region of joints after soldering Cu–15μm Sn–Cu sandwich structure at 260 °C, 0.04 MPa, 40 h

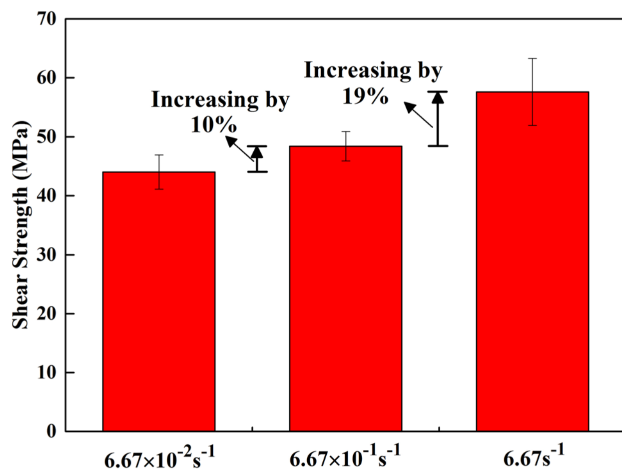

Fig. 7 Shear strength of $Cu/Cu_3Sn/Cu$ joints under different strain rates

consumed, and the interfacial region of joints was completely composed of Cu_3Sn. It was confirmed that the $Cu/Cu_3Sn/Cu$ joints were obtained after the soldering of 260 °C, 0.04 MPa, and 40 h. Moreover, it was also known that the connected status of $Cu/Cu_3Sn/Cu$ joints was well because of no defect (e.g., the local unconnected defect) in the interfacial region (Fig. 5a).

Figure 7 gives the shear strength of $Cu/Cu_3Sn/Cu$ joints under the strain rates of 6.67×10^{-2} s^{-1}, 6.67×10^{-1} s^{-1} and 6.67 s^{-1}. The shear strength of $Cu/Cu_3Sn/Cu$ joints was 44 MPa under the strain rate of 6.67×10^{-2} s^{-1}. As the strain rate increased to 6.67×10^{-1} s^{-1}, the shear strength of joints increased to 48.4 MPa. Compared with the strength under 6.67×10^{-2} s^{-1}, the strength of joints under 6.67×10^{-1} s^{-1} increased by 10%. Then, with the strain rate increasing to 6.67 s^{-1}, the strength of joints further increased to 57.6 MPa, which increased by 19% in comparison with the strength under 6.67×10^{-1} s^{-1}. Therefore, the shear strength of $Cu/Cu_3Sn/Cu$ joints increased gradually when the strain rate was 6.67×10^{-2} s^{-1}, 6.67×10^{-1} s^{-1} , and 6.67 s^{-1}. It was thought that the intensification of work-hardening effect had caused the increased strength of joints with the strain rate increasing from 6.67×10^{-2} s^{-1} to 6.67 s^{-1}. According to the literature [23–25], it is known dislocation density within interfacial region of joints increases as the increase of strain rates, which means intersection and pinning happen among an increasing number of dislocations within interfacial region. Under this case, the interfacial region has more remarkable work-hardening effect, which further leads to the increase of joints strength.

Figure 8 gives the stress–strain curves of $Cu/Cu_3Sn/Cu$ joints under the strain rates of 6.67×10^{-2} s^{-1}, 6.67×10^{-1} s^{-1}, and 6.67 s^{-1}. When the strain rate was, respectively, 6.67×10^{-2} s^{-1}, 6.67×10^{-1} s^{-1} , and 6.67 s^{-1}, there was no obvious stage of plastic deformation for the stress–strain curves. After stress arrived at peak points, it declined quite rapidly with the increase of strain. In other words, the stress–strain curves of joints under these strain rates all presented typical characteristics of brittle fracture. Moreover, as the strain rate increasing from 6.67×10^{-2} s^{-1} to 6.67 s^{-1}, the joints' ability for resisting elastic deformation gradually increased, which indicated the stiffness of joints gradually magnified. It was considered that the increase of stiffness also resulted from the intensification of work-hardening effect within interfacial region.

3.2 Fracture mechanism of $Cu/Cu_3Sn/Cu$ joints under different strain rates

Figure 9 gives the cross-sectional fractured morphologies of $Cu/Cu_3Sn/Cu$ joints under the strain rates of 6.67×10^{-2} s^{-1}, 6.67×10^{-1} s^{-1} , and 6.67 s^{-1}. As shown in Fig. 9, when the strain rate was 6.67×10^{-2} s^{-1}, 6.67×10^{-1} s^{-1} , and 6.67 s^{-1} , respectively, Cu substrates were all covered by Cu_3Sn in the cross-sectional fractured morphologies. It should be noted that the Cu_3Sn on Cu substrates had uniform thickness with the strain rates of 6.67×10^{-2} s^{-1} and 6.67×10^{-1} s^{-1} (Fig. 9a, b). However, after the joints fractured under the strain rate of 6.67 s^{-1}, the Cu_3Sn on Cu substrates could be divided into two parts with different thickness (Fig. 9c). The two parts, respectively, had uniform thickness, and the thickness difference between them resulted in the appearance of obvious step. Therefore, it was thought that fractured path did not divert when the $Cu/Cu_3Sn/Cu$ joints fractured under the strain rates of 6.67×10^{-2} s^{-1} and 6.67×10^{-1} s^{-1}, while there was diversion regarding the fractured path for the strain rate of 6.67 s^{-1}.

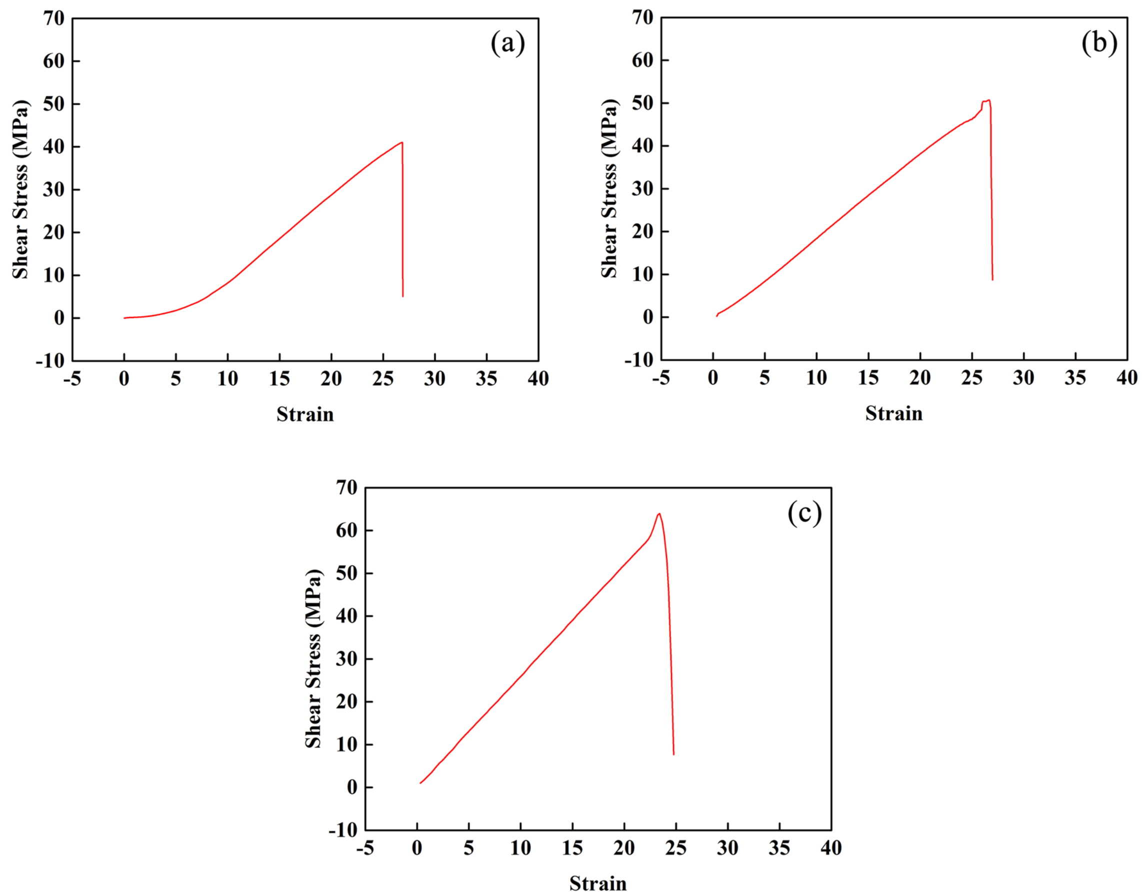

Fig. 8 Stress–strain curves of Cu/Cu_3Sn/Cu joints under different strain rates. **a** 6.67×10^{-2} s^{-1} **b** 6.67×10^{-1} s^{-1} **c** 6.67 s^{-1}

Figure 10 shows the thickness of Cu_3Sn in the cross-sectional fractured morphologies under different strain rates. With the strain rates of 6.67×10^{-2} s^{-1} and 6.67×10^{-1} s^{-1}, the Cu_3Sn on Cu substrates, respectively, had thickness of 4.6 µm and 4.7 µm. As the strain rate increased to 6.67 s^{-1}, the thickness of thin part of Cu_3Sn was merely 0.6 µm, while the thick part of Cu_3Sn had thickness of 2.6 µm. The interconnected height for fabricating Cu/Cu_3Sn/Cu joints was 15 µm (Fig. 1), which was larger than the Cu_3Sn thickness in these fractured morphologies. It was thus inferred that the fracture of Cu/Cu_3Sn/Cu joints all happened within Cu_3Sn under these strain rates.

Figure 11 gives the top-view fractured morphologies of Cu/Cu_3Sn/Cu joints under the strain rates of 6.67×10^{-2} s^{-1}, 6.67×10^{-1} s^{-1} , and 6.67 s^{-1}. It should be noted that Fig. 11d, f, respectively, present the magnified morphologies marked by red rectangular boxes in Fig. 11c, e. As shown in Fig. 11, no obvious plastic deformation could be observed in the top-view fractured morphologies, which indicated that the fracture of Cu/Cu_3Sn/Cu joints all belonged to brittle fracture under these strain rates. When the strain rates were 6.67×10^{-2} s^{-1} and 6.67×10^{-1} s^{-1}, the fractured surface was relatively planar (Fig. 11a–d). The fractured surface with planar shape suggested the Cu_3Sn covered on Cu substrates had uniform thickness. It was further known that there was no diversion regarding the fractured path of joints under these two strain rates. However, with the strain rate of 6.67 s^{-1}, the fractured surface presented stepladder-like shape, indicating the thickness of Cu_3Sn covered on Cu substrates was not uniform, and the fractured path of joints diverted (Fig. 11e, f). Undoubtedly, these characteristics in Fig. 11 complied with what had been inferred based on the stress–strain curves (Fig. 8), as well as the cross-sectional fractured morphologies (Fig. 9).

The top-view fractured morphologies of joints were composed of exposed Cu_3Sn grains and broken Cu_3Sn grains for the strain rate of 6.67×10^{-2} s^{-1} (Fig. 11a, b). The appearance of broken Cu_3Sn grains meant transgranular fracture happened within Cu_3Sn. However, there was no feather of transgranular fracture on the exposed Cu_3Sn grains, which demonstrated the occurrence of intergranular fracture. As a result, it was known that a mixture of transgranular fracture and intergranular fracture happened within joints when the strain rate was 6.67×10^{-2} s^{-1}. Similar to the top-view

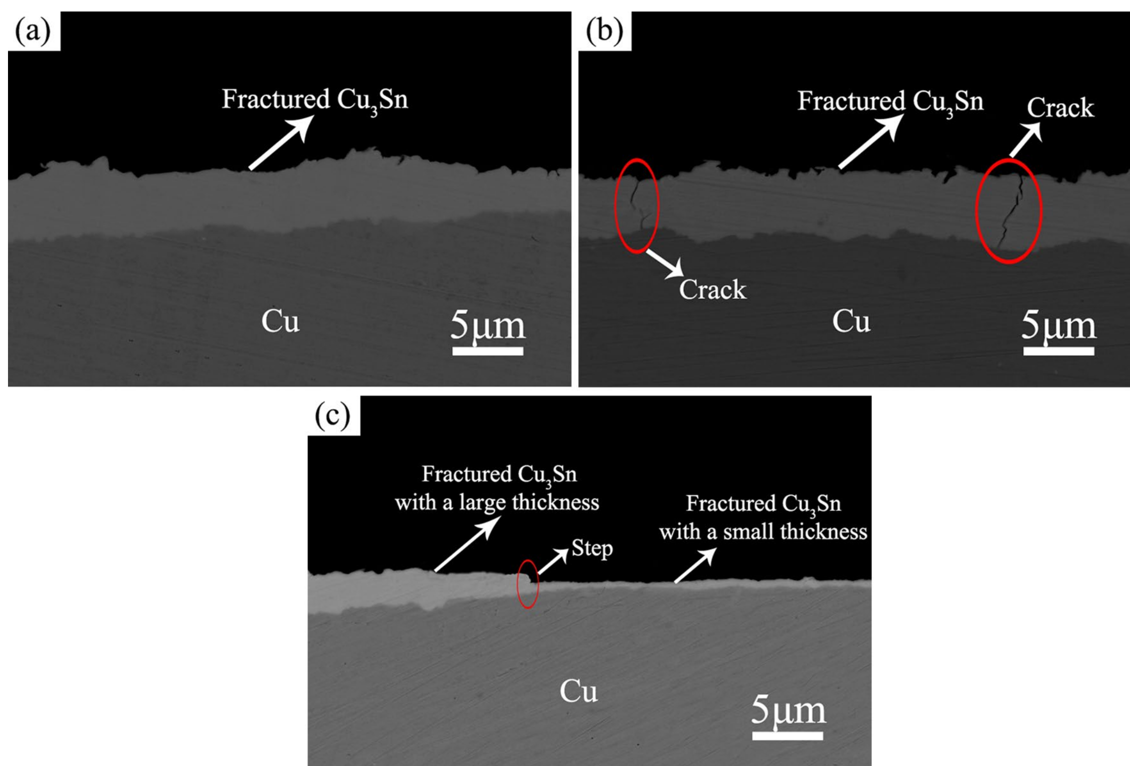

Fig. 9 Cross-sectional fractured morphologies of Cu/Cu_3Sn/Cu joints under different strain rates. **a** 6.67×10^{-2} s^{-1} **b** 6.67×10^{-1} s^{-1} **c** 6.67 s^{-1}

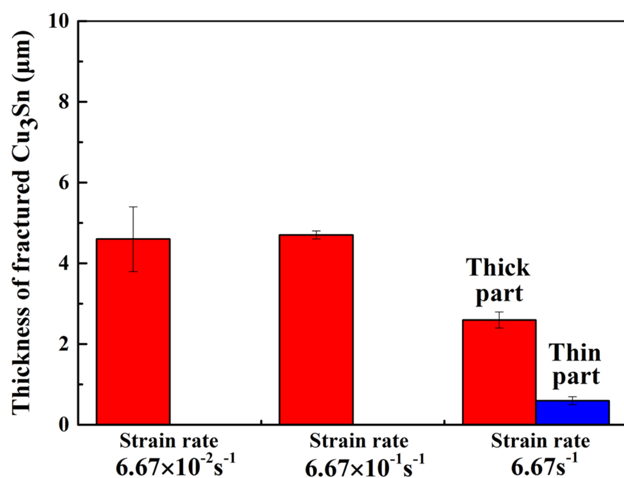

Fig. 10 Thickness of Cu_3Sn in cross-sectional fractured morphologies under different strain rates

fractured morphologies of 6.67×10^{-2} s^{-1}, the fractured morphologies of 6.67×10^{-1} s^{-1} were also composed of exposed Cu_3Sn grains and broken Cu_3Sn grain (Fig. 11c, d). This led to a fact that the fracture of joints under 6.67×10^{-1} s^{-1} was also the mixture of transgranular fracture and intergranular fracture. Compared with the fracture of 6.67×10^{-2} s^{-1}, the fracture of 6.67×10^{-1} s^{-1} involved that the transgranular fracture happened at more positions within joints. It should be noted that the fractured surface of each broken Cu_3Sn grain was one cleavage plane for the strain rate of 6.67×10^{-2} s^{-1} or 6.67×10^{-1} s^{-1}. Therefore, under these two strain rates, the transgranular fracture happened actually belonged to cleavage fracture. Crack had propagated along cleavage planes during the transgranular fracture.

When the strain rate was 6.67 s^{-1}, the top-view fractured morphologies were completely composed of broken Cu_3Sn grains, which indicated only transgranular fracture within Cu_3Sn happened for joints (Fig. 11e, f). For the fractured surfaces of some Cu_3Sn grains, they were, respectively, one cleavage plane. On the fractured surfaces of other Cu_3Sn grains, cleavage step as well as river pattern could be observed. This suggested that crack had passed a series of parallel cleavage planes during propagating within these Cu_3Sn grains. In addition to cleavage planes, it is known that cleavage step and river pattern are also typical characteristics of cleavage fracture. Therefore, similar to the transgranular fracture of 6.67×10^{-2} s^{-1} and 6.67×10^{-1} s^{-1}, the transgranular fracture of 6.67 s^{-1} also belonged to cleavage fracture. As shown in Fig. 11e, f, it could be also seen that there existed ridge between different regions of Cu_3Sn grains, which was due to the height difference of these

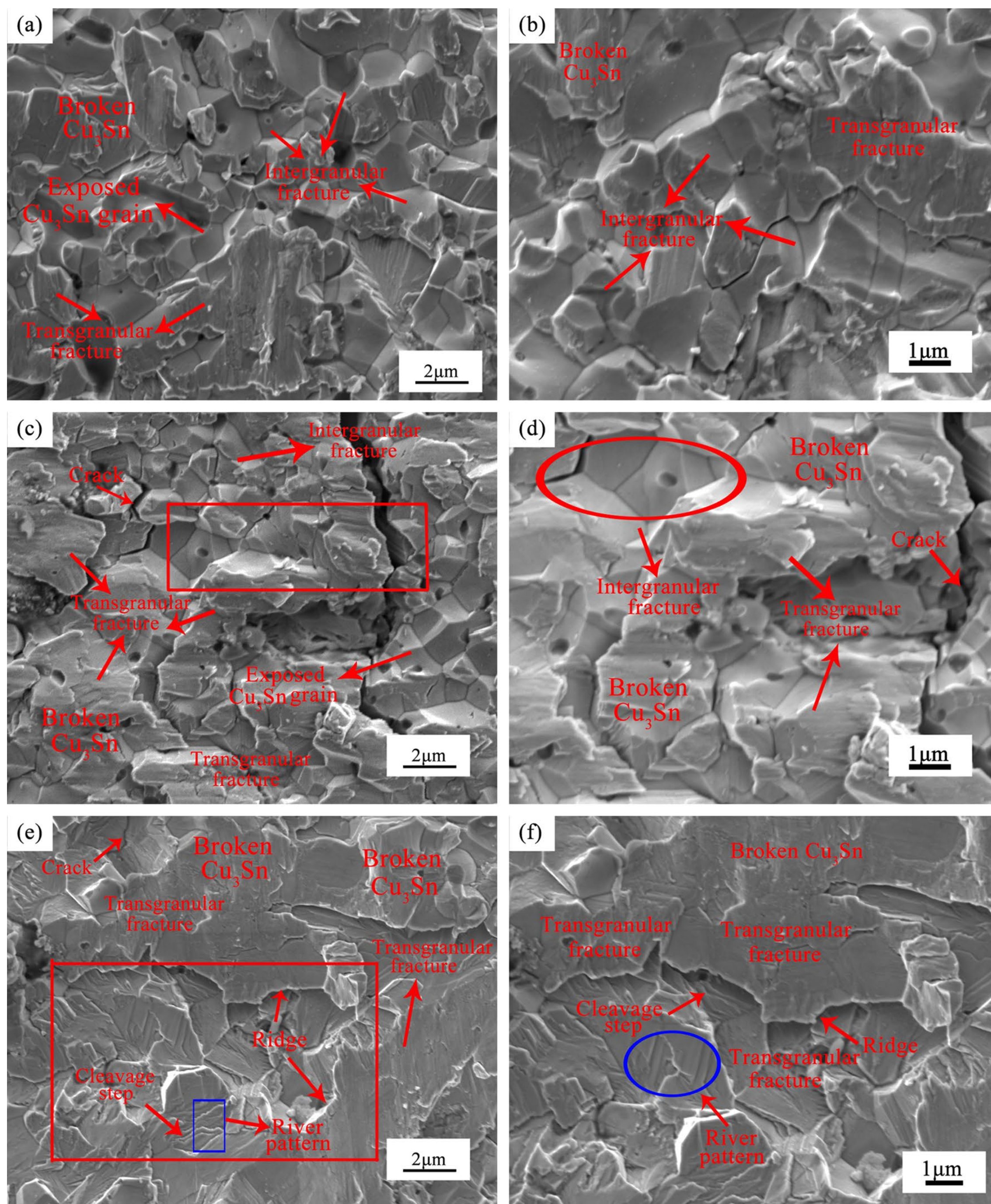

Fig. 11 Top-view fractured morphologies of Cu/Cu_3Sn/Cu joints under different strain rates. **a**, **b** 6.67×10^{-2} s^{-1} **c**, **d** 6.67×10^{-1} s^{-1} **e**, **f** 6.67 s^{-1}

regions. The appearance of ridge was consistent with the formation of step in corresponding cross-sectional fractured morphologies (Fig. 9c).

In Fig. 9 or in Fig. 11, some microcrack could be seen within Cu_3Sn. It was considered that the inherent brittleness of Cu_3Sn was the root cause for forming the microcrack. As mentioned above, the proportion of transgranular fracture increased with the strain rate increasing from 6.67×10^{-2} s^{-1} to 6.67 s^{-1}, which resulted in the proportion of intergranular fracture declining simultaneously. This could be also proved through quantitatively analyzing the proportion of different fracture under these strain rates, as shown in Fig. 12. For the strain rate of 6.67 s^{-1}, the proportion of transgranular fracture reached 100%. When the strain rate increased from

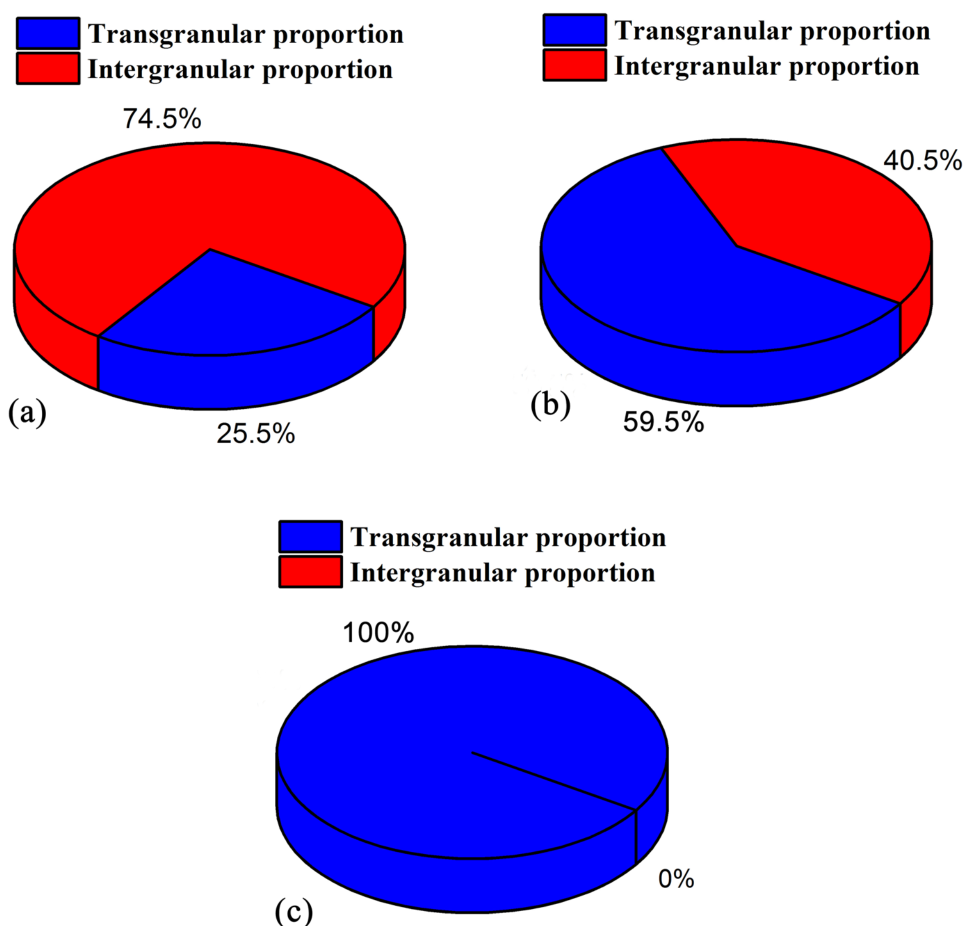

Fig. 12 Proportion of transgranular fracture and intergranular fracture for $Cu/Cu_3Sn/Cu$ joints under different strain rates. **a** 6.67×10^{-2} s^{-1} **b** 6.67×10^{-1} s^{-1} **c** 6.67 s^{-1}

6.67×10^{-2} s^{-1} to 6.67×10^{-1} s^{-1}, the proportion of transgranular fracture increased from 25.5% to 59.5%, and the proportion of intergranular fracture decreased from 74.5% to 40.5%.

3.3 Effects of fracture mechanism on crack propagation

Through analyzing the fractured path and fractured type, the fracture mechanism of $Cu/Cu_3Sn/Cu$ joints under different strain rates was revealed, and Fig. 13 presents the schematic illustration of fracture mechanism. For the strain rates of 6.67×10^{-2} s^{-1} and 6.67×10^{-1} s^{-1}, the fracture of $Cu/Cu_3Sn/Cu$ joints was both the mixture of transgranular fracture and intergranular fracture, while the fractured path both kept continuous without diversion (Fig. 13a, b). Nevertheless, under the strain rate of 6.67 s^{-1}, the fracture happened completely belonged to transgranular fracture, and the fractured path diverted with the formation of step in the meantime (Fig. 13c).

According to the fractured theory of metals [26, 27], it is known that crack needs to obtain energy when propagating within metals, which is due to the continuous formation of new plastic-deformation zones in crack tip. In other words, the energy obtained for crack is consumed in the formation of plastic-deformation zones during crack propagating within metals. The work, needed to be done when forming plastic-deformation zones, acts as resistance for crack propagation. Only when the energy obtained is larger than the resistance, the crack propagation can happen [26]. It is therefore considered that the more energy obtained indicates the larger resistance during crack propagation.

Actually, during crack propagation, the continuous formation of plastic-deformation zones is realized through dislocation slip in crack tip. If the dislocation slip is easy to happen, the plastic-deformation zones in crack tip is easy to form. This leads to small propagation resistance of crack. For the transgranular fracture, crack needs to transverse grain boundary between different grains. When the crack propagates to grain boundary, the grain boundary acts as obstacle for the dislocation slip in crack tip. This results in the formation of dislocation pile-up around the grain boundary. With the dislocation pile-up, it is tough for the dislocation slip, which causes difficulty in forming plastic-deformation zones in crack tip. However, when the intergranular fracture happens, crack propagates along

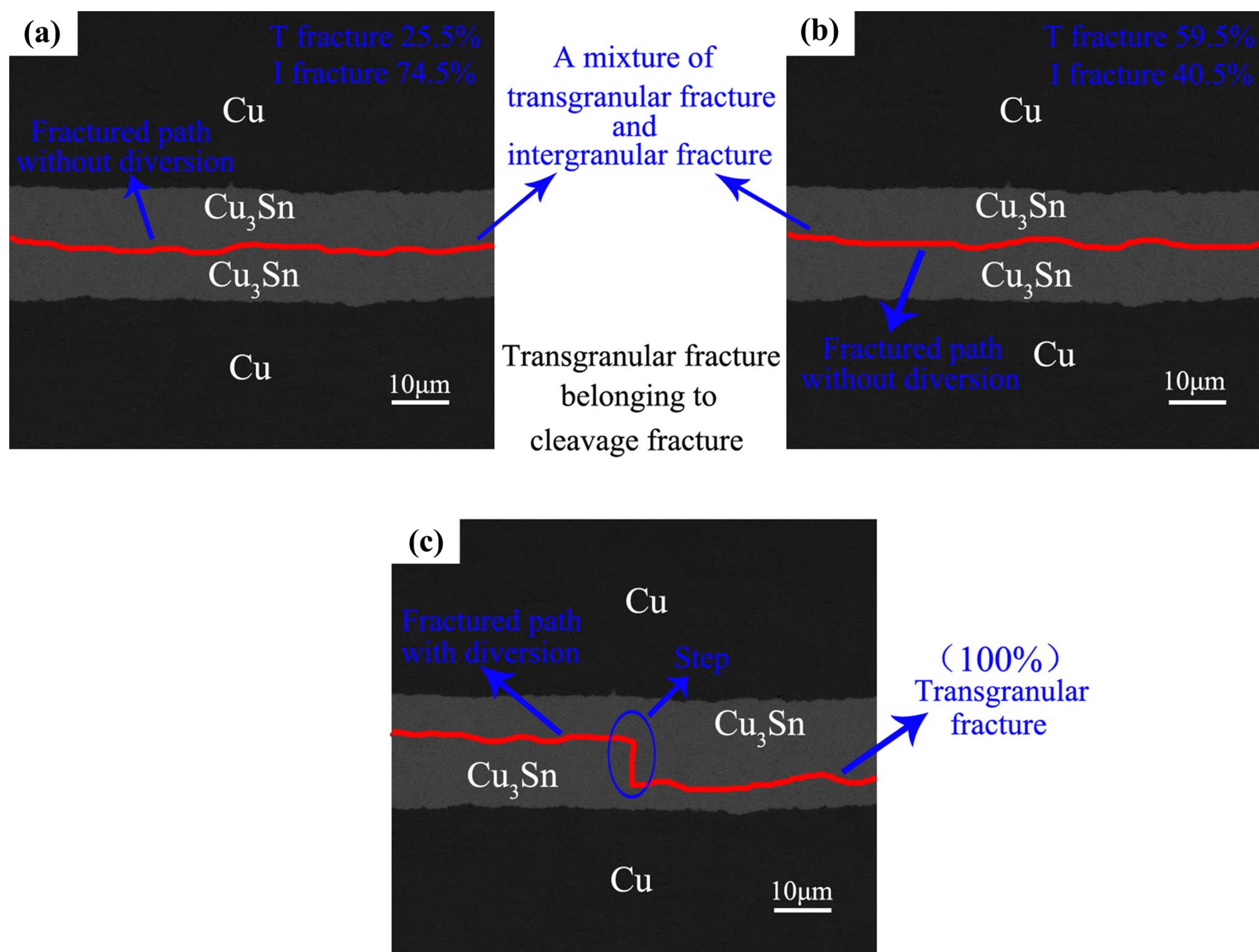

Fig. 13 Schematic illustration of fracture mechanism for $Cu/Cu_3Sn/Cu$ joints under different strain rates. **a** 6.67×10^{-2} s^{-1} **b** 6.67×10^{-1} s^{-1} **c** 6.67 s^{-1}

grain boundary all the time, and there is no need for the crack to transverse the grain boundary. Under this case, the dislocation slip in crack tip cannot be impeded by the grain boundary. It can be seen the dislocation slip in crack tip is easier to happen for the intergranular fracture compared with the transgranular fracture. Thus, the plastic-deformation zones of intergranular fracture are easier to form. The easier formation of plastic-deformation zones means smaller propagation resistance of crack for the intergranular fracture in comparison with that for the transgranular fracture. With the strain rates of 6.67×10^{-2} s^{-1}, 6.67×10^{-1} s^{-1} , and 6.67 s^{-1}, the proportion of transgranular fracture gradually increased (25.5%, 59.5%, 100%), while the proportion of intergranular fracture correspondingly decreased (74.5%, 40.5%, 0), as shown in Figs. 11, 12, 13. When the proportion and crack propagation resistance of different fracture were taken into consideration, it was thought the propagation resistance of crack increased when the strain rate was 6.67×10^{-2} s^{-1}, 6.67×10^{-1} s^{-1} , and 6.67 s^{-1}.

For 6.67×10^{-2} $s^{-1}\rightarrow6.67\times10^{-1}$ s^{-1} and 6.67×10^{-1} $s^{-1}\rightarrow6.67$ s^{-1}, the proportion of transgranular fracture, respectively, increased by 34% and 40.5%, which indicated a roughly equal increased amplitude. Therefore, when merely considering the fractured type under different strain rates, the increased amplitude of crack propagation resistance should be nearly the same for 6.67×10^{-2} $s^{-1}\rightarrow6.67\times10^{-1}$ s^{-1} and 6.67×10^{-1} $s^{-1}\rightarrow6.67$ s^{-1}. It was impossible to ignore a fact that there also existed difference regarding the fractured path under different strain rates (Figs. 9, 11 and 13). The fractured path kept continuous under 6.67×10^{-2} s^{-1} and 6.67×10^{-1} s^{-1}, while diversion happened on the fractured path of 6.67 s^{-1}. According to the literature [27], it is also learnt that the propagation resistance for crack increases when the fractured path diverts and does not keep continuous. Compared with 6.67×10^{-2} s^{-1} and 6.67×10^{-1} s^{-1}, the diversion of fractured path under

6.67 s^{-1} resulted in the increase of propagation resistance for crack as well. Overall, with the consideration of fracture mechanism (fractured type and fractured path), it was inferred the increase of crack propagation resistance for 6.67×10^{-1} $s^{-1}\rightarrow6.67$ s^{-1} was at a larger amplitude than that for 6.67×10^{-2} $s^{-1}\rightarrow6.67\times10^{-1}$ s^{-1}.

It has been pointed out that crack requiring more energy during propagation means larger propagation resistance. Actually, the acquired energy during crack propagation derives from released elastic energy during fracture [26]. In other words, the propagation resistance for crack can be reflected through the released elastic energy during fracture. The released elastic energy per unit volume can be calculated based on stress–strain curves during fracture. Figure 14 describes the method to calculate the released elastic energy per unit volume according to the stress–strain curve. Two lines, which are, respectively, parallel to the elastic zone and vertical to the strain axis, are made from the peak point of curves. Both the lines should intersect with the strain axis, leading to the formation of triangle between the lines and strain axis. The area of triangle is regarded as the released elastic energy per unit volume. With this method, the released elastic energy of $Cu/Cu_3Sn/Cu$ joints under different strain rates was calculated, which was on the basis of strain–stress curves in Fig. 8. It should be noted that the elastic zone of stress–strain curves under ideal status is a line across the zero point of coordinate system. However, the elastic zone of stress–strain curves from practical shear test is not a line, but a curve approximated to a line. Therefore, linear fitting crossing zero points was done for the elastic zone in Fig. 8. After the fitted lines were obtained, their parallel lines were made from peak points for calculating the released elastic energy of joints.

Through calculation, the released elastic energy per unit volume of joints was finally acquired, as shown in Fig. 15.

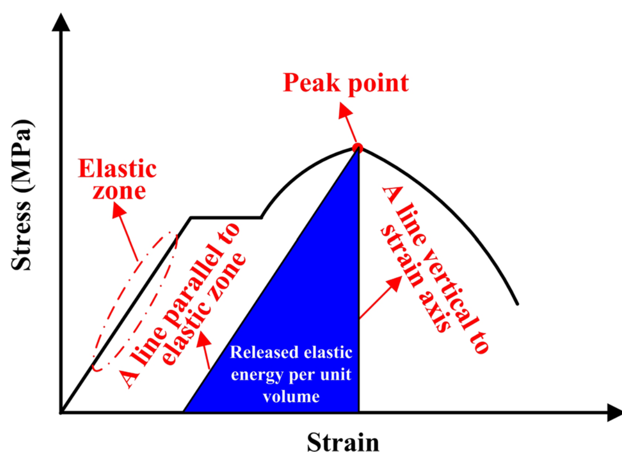

Fig. 14 Method for calculating released elastic energy per unit volume based on stress–strain curves

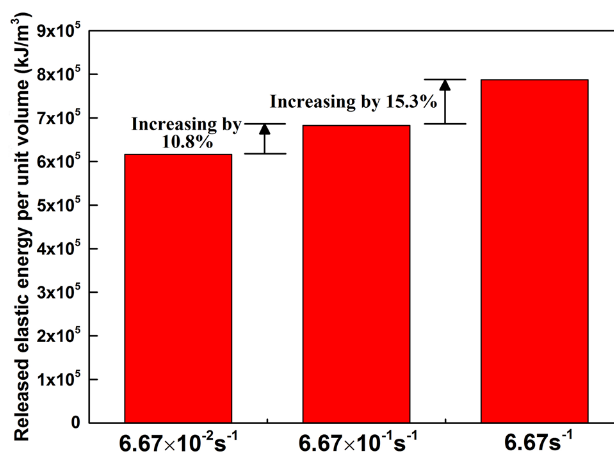

Fig. 15 Released elastic energy per unit volume of $Cu/Cu_3Sn/Cu$ joints under different strain rates

When the strain rate was, respectively, 6.67×10^{-2} s^{-1}, 6.67×10^{-1} s^{-1}, and 6.67 s^{-1}, the released elastic energy per unit volume presented an ascending trend. As the strain rate increasing from 6.67×10^{-2} s^{-1} to 6.67×10^{-1} s^{-1}, the released elastic energy of joints increased by 10.8%. Comparatively, for the strain rate changing from 6.67×10^{-1} s^{-1} to 6.67 s^{-1}, the increase of released elastic energy was at a larger amplitude(15.3%). According to the released elastic energy of joints, it was confirmed that the increase of crack propagation resistance during fracture was at a larger extent for 6.67×10^{-1} $s^{-1}\rightarrow6.67$ s^{-1} in comparison with that for 6.67×10^{-2} $s^{-1}\rightarrow6.67\times10^{-1}$ s^{-1}. Further, this also proved the effect of fracture mechanism on crack propagation we had discussed.

3.4 Strain rate sensitivity of $Cu/Cu_3Sn/Cu$ Joints

The strain rate sensitivity of metals not only represents the ability to resist necking, but also correlates with thermal fatigue resistance closely [24, 28]. Under this case, several researchers have conducted the studies related to strain rate sensitivity [22, 25, 28–31]. However, it should be noted that some of these studies were merely carried out on bulk solder specimens rather than real solder joints configuration [28–30]. Although there are other studies focusing on the strain rate sensitivity of solder joints [22, 25, 31], only the conventional joints were involved in these studies. This means there has been no study about the strain rate sensitivity of full IMCs joints yet. The strain rate sensitivity of joints is an important part for reliabilities, and there must be difference of strain rate sensitivity between full IMCs joints and conventional joints. As shown in Fig. 7, the shear strength of $Cu/Cu_3Sn/Cu$ joints increased continuously with the strain rate increasing from 6.67×10^{-2} s^{-1} to 6.67 s^{-1}, which demonstrated the strength of $Cu/Cu_3Sn/Cu$ joints

depended remarkably on the strain rate. Consequently, the strain rate sensitivity of $Cu/Cu_3Sn/Cu$ joints was analyzed on the basis of shear strength under different strain rates.

According to the literature [22, 25, 28–31], it is known that the strength (σ) and the strain rate (ε) can be expressed as.

$$\sigma = A\varepsilon^m, \tag{1}$$

where A is one constant and m is the strain rate sensitivity index. The strain rate sensitivity index (m) actually describes the strain rate sensitivity. Then, one can get.

$$\lg \sigma = \lg A + m \lg \varepsilon. \tag{2}$$

So the strength (σ) and the strain rate (ε) present a linear relationship under log–log coordinate. Figure 16 shows the relationship between the strength of $Cu/Cu_3Sn/Cu$ joints and the strain rate under log–log coordinate. Through linear fitting, the strain rate sensitivity index (m) of $Cu/Cu_3Sn/Cu$ joints was determined to be 0.058. Table 1 gives the strain rate sensitivity index of $Cu/Cu_3Sn/Cu$ joints, as well as conventional joints derived from Cu/Sn-based solder system. As shown in Table 1, the strain sensitivity rate index of conventional joints are all larger than 0.058 [22, 25, 31]. It was known that the strain rate sensitivity of $Cu/Cu_3Sn/Cu$ joints was smaller than that of conventional joints. Compared with the conventional joints, the $Cu/Cu_3Sn/Cu$ joints had smaller resistance to necking and thermal fatigue.

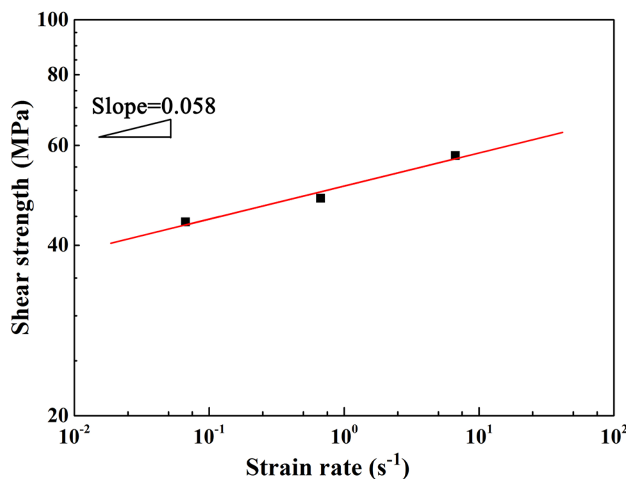

Fig. 16 Relationship between strength of $Cu/Cu_3Sn/Cu$ joints and strain rate

The $Cu/Cu_3Sn/Cu$ joints and the conventional joints have different interfacial structure. Then, we considered that the distinction of interfacial structure had led to the difference in the strain rate sensitivity. Figure 17 presents the schematic illustration of interfacial structure for two joints. For the conventional joints, they have the interfacial structure of Cu/Cu–Sn IMCs/residual Sn-based solder/Cu–Sn IMCs/Cu. As shown in Fig. 17a, the residual solder occupies quite a large proportion in the interfacial region, while the IMCs merely occupy quite a small proportion. Because of the great ductility of residual solder [30, 32, 33], the conventional joints have large strain rate sensitivity. However, for the $Cu/Cu_3Sn/Cu$ joints, there is no residual solder in the interfacial region, and the interfacial region is totally composed of Cu_3Sn, as shown in Fig. 17b. Due to the natural brittleness of Cu–Sn IMCs, Cu_3Sn has poor ductility compared with the residual solder. When external loads are applied on solder joints, the fracture is certain to happen in the interfacial region [34–37]. Therefore, as the strain rates increase, stress concentration is easier to occur in Cu_3Sn of $Cu/Cu_3Sn/Cu$ joints in comparison with residual solder of conventional joints. The easier happening of stress concentration further causes easier initiation and propagation of crack in Cu_3Sn of $Cu/Cu_3Sn/Cu$ joints. When the strain rate is at the same increment, the strength of conventional joints increases more remarkably than that of $Cu/Cu_3Sn/Cu$ joints. Finally, this results in the $Cu/Cu_3Sn/Cu$ joints having the smaller strain rate sensitivity.

Under the strain rates of 6.67×10^{-2} s^{-1}, 6.67×10^{-1} s^{-1}, and 6.67 s^{-1}, the shear strength of $Cu/Cu_3Sn/Cu$ joints was, respectively, 44 MPa, 48.4 MPa, and 57.6 MPa (Fig. 7). However, for the conventional joints, the shear strength ranges from 10 to 30 MPa [38–43]. It was therefore thought that the $Cu/Cu_3Sn/Cu$ joints had larger strength in comparison with the conventional joints. Actually, the strength of solder joints depends on the strength of interfacial region, which is due to the fracture occurring within interfacial region under external loads. Because of the nonuniformity of interfacial region, the position, at which the fracture

Table 1 Strain rate sensitivity index of $Cu/Cu_3Sn/Cu$ joints and conventional joints derived from Cu/Sn-based solder system

Joints type	Solder	Strain rate sensitivity index (m)	Linear correlation coefficient (R^2)	Joints type	Solder	Strain rate sensitivity index (m)	Linear correlation coefficient (R^2)
$Cu/Cu_3Sn/Cu$ joints	Pure Sn	0.058	0.945	Conventional joints [22, 25, 31]	Sn–3.5Ag [25]	0.076–0.087 [25]	0.99 [25]
					Sn–3.5Ag [31]	0.085–0.1 [31]	–
					Sn3.0Ag0.5Cu [22]	0.078, 0.089 [22]	–

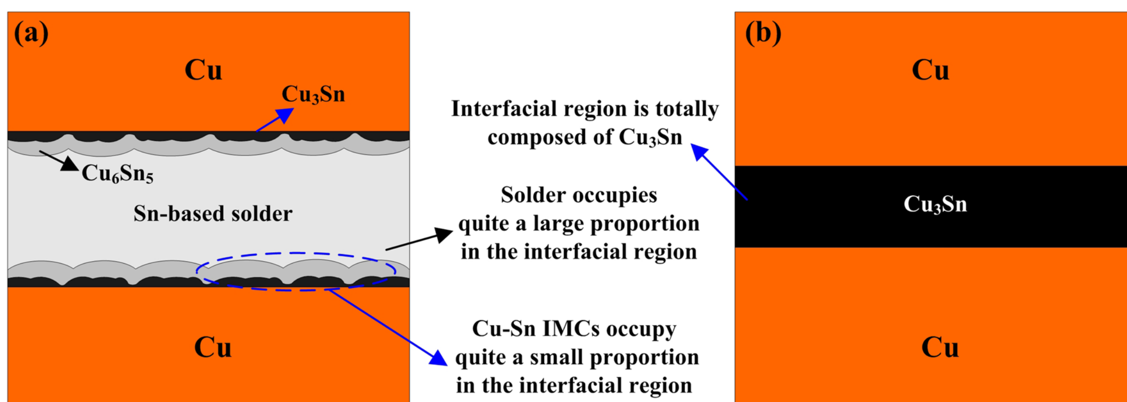

Fig. 17 Schematic illustration of interfacial structure for $Cu/Cu_3Sn/Cu$ joints and conventional joints. **a** Conventional joints **b** $Cu/Cu_3Sn/Cu$ joints

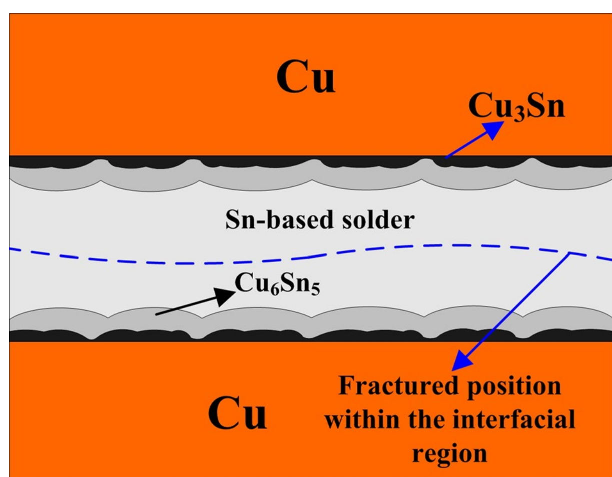

Fig. 18 Schematic illustration of fractured position within interfacial region of conventional joints

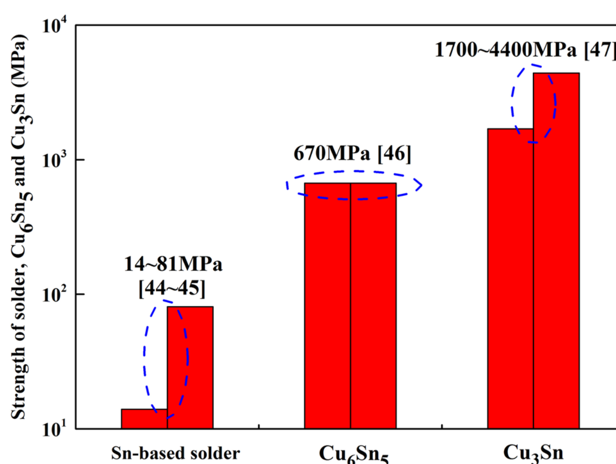

Fig. 19 Strength of Sn-based solder, Cu_6Sn_5 and Cu_3Sn [44–47]

happens within interfacial region, determines the strength of interfacial region. When the fracture happens among phases of high strength within interfacial region, the strength of interfacial region is high. With the large strength of interfacial region, the strength of joints is bound to be high.

Figure 18 shows the schematic illustration describing the fractured position within interfacial region of conventional joints. As shown in Fig. 18, the fracture of conventional joints totally happens within the residual solder [38–40]. The interfacial structure of conventional joints has led to the fracture within residual solder, which results from the residual solder taking up quite a large proportion in the interfacial region. For the $Cu/Cu_3Sn/Cu$ joints, it was found that the fracture completely happened within Cu_3Sn (Fig. 13). The interfacial region of $Cu/Cu_3Sn/Cu$ joints is totally composed of Cu_3Sn, and this causes the occurrence of fracture within Cu_3Sn. Based on the literature [44–47], it is known that the strength of Sn-based solder, Cu_6Sn_5 and Cu_3Sn, presents an increasing trend, as shown in Fig. 19. For the Sn-based solder, the strength ranges from 14 to 81 MPa [44, 45]. In comparison with the solder, the strength of Cu_6Sn_5 increases largely to 670 MPa [46], and then the strength of Cu_3Sn further increases to 1700–4400 MPa [47]. Therefore, it was considered the difference of fractured position resulted in the strength difference of two joints.

4 Conclusions

In this study, $Cu/Cu_3Sn/Cu$ joints were fabricated from Cu–15μm Sn–Cu sandwich structure, and shear fracture of $Cu/Cu_3Sn/Cu$ joints under different strain rates was systematically analyzed.

When the strain rate was 6.67×10^{-2} s^{-1}, 6.67×10^{-1} s^{-1}, and 6.67 s^{-1}, $Cu/Cu_3Sn/Cu$ joints, respectively, had the shear

strength of 44 MPa, 48.4 MPa, and 57.6 MPa, and the stiffness of joints also gradually increased. The intensification of work-hardening effect within interfacial region resulted in the increased strength and stiffness.

Under 6.67×10^{-2} s^{-1} and 6.67×10^{-1} s^{-1}, the fractured path of joints both kept continuous without diversion in Cu_3Sn, and the fracture both belonged to a mixture of transgranular fracture and intergranular fracture. As the strain rate increasing from 6.67×10^{-2} s^{-1} to 6.67×10^{-1} s^{-1}, the proportion of transgranular fracture increased from 25.5% to 59.5%, while the proportion of intergranular fracture declined from 74.5% to 40.5% accordingly. Under 6.67 s^{-1}, the fracture of joints merely belonged to transgranular fracture within Cu_3Sn, while the fractured path diverted with the formation of step. Actually, the transgranular fracture of different strain rates was cleavage fracture.

The crack propagation resistance increased by a larger amplitude for 6.67×10^{-1} s$^{-1}\rightarrow6.67$ s^{-1} compared with that for 6.67×10^{-2} s$^{-1}\rightarrow6.67\times10^{-1}$ s^{-1}, which was due to the fracture mechanism of different strain rates. The released elastic energy of joints proved the effect of fracture mechanism on crack propagation.

Compared with conventional joints, $Cu/Cu_3Sn/Cu$ joints had smaller strain rate sensitivity. The different interfacial structure of two joints caused the difference in the strain rate sensitivity. Besides, the strength of $Cu/Cu_3Sn/Cu$ joints was larger than that of conventional joints, which resulted from the difference in fractured position of two joints.

Acknowledgements This investigation was supported by National Natural Science Foundation of China under the grant of No. 51575011 and No.51975013, Beijing Natural Science Foundation under the grant of No. 2162002.

References

1. J. Pei, L. Deng, S. Song, M.G. Zhao, Y.H. Zhang, S. Wu, G.R. Wang, Z. Zhu, Z.Z. Wu, W. He, F. Chen, N. Deng, S. Wu, N. Deng, S. Wu, Y. Wang, Y.J. Wu, Z.Y. Yang, Y.J. Wu, Z.Y. Yang, C. Ma, G.Q. Li, W.T. Han, H.L. Li, H.Q. Wu, R. Zhao, Y. Xie, L.P. Shi, Nature **572**, 106 (2019)
2. Y. C. Kim, D. J. Shin, J. S. Lee, Y. S. Lee, H. J. Yoo, IEEE International Solid-State Circuits Conference, San Francisco, USA. 258 (2016)
3. G. Lacey, G. Taylor, S. Areibi, Available online at: https://arxiv.org/abs/1602.04283
4. C. Dong, G.R. He, X.M. Liu, Y. Yang, W.Z. Guo, IEEE Access **7**, 23628 (2019)
5. M.B. Tian, *Electronic Packaging Technology* (Tsinghua University Press, Beijing, 2003)
6. H. Ardebili, M. Pecht, *Encapsulation Technologies for Electronic Applications* (Elsevier, Burlington, 2009)
7. M. Pecht, *Handbook of Electronic Package Design* (Marcel Dekker, New York, 1991)
8. G. Harman, *Wire Bonding in Microelectronics*, 3rd edn. (McGraw-Hill, New York, 2010)
9. B.L. Liu, Y.H. Tian, J.Y. Feng, C.X. Wang, J. Mater. Sci. **52**, 1943 (2017)
10. M. L. Huang, X. L. Hou, H. T. Ma, J. Zhao, Y. C. Yang, 14th International Conference on Electronic Packaging Technology, Dalian, China. 879(2013)
11. F.J. Wang, Y. Huang, Z.J. Zhang, C. Yan, Materials **10**, 920 (2017)
12. J. Q. Huang, M. B. Zhou, X. P. Zhang, 17th International Conference on Electronic Packaging Technology, Wuhan, China. 968(2016)
13. S. Li, Y.F. Yan, J. Mater. Sci. **26**, 9470 (2015)
14. T. Xu, X.W. Hu, Y.L. Li, X.X. Jiang, J. Mater. Sci. **28**, 18515 (2017)
15. X. Deng, R.S. Sidhu, P. Johnson, N. Chawla, Matal. Mater. Trans. A **36A**, 55 (2005)
16. Y.L. Huang, Z.Y. Xiu, G.H. Wu, Y.H. Tian, H. Peng, X.L. Gu, W.M. Long, Mater. Lett. **169**, 262 (2016)
17. C.J. Hang, Y.H. Tian, R. Zhang, D.S. Yang, J. Mater. Sci. **24**, 3905 (2013)
18. J.F. Li, P.A. Agyakwa, C.M. Johnson, Acta. Mater. **59**, 1198 (2011)
19. H.J. Dong, Z.L. Li, X.G. Song, H.Y. Zhao, J.C. Yan, H. Tian, J.H. Liu, J. Alloys Compd. **723**, 1026 (2017)
20. H.J. Dong, Z.L. Li, X.G. Song, H.Y. Zhao, H. Tian, J.H. Liu, J.C. Yan, Mater. Sci. Eng. A. **705**, 360 (2017)
21. H.K. Shao, A.P. Wu, Y.D. Bao, Y. Zhao, G.S. Zou, Mater. Sci. Eng. A. **680**, 221 (2017)
22. X.W. Hu, T. Xu, L.M. Keer, Y.L. Li, X.X. Jiang, J. Alloys Compd. **690**, 720 (2017)
23. G.X. Hu, X. Cai, *Fundamentals of Materials Science* (Shanghai Jiaotong University Press, Shanghai, 2000)
24. C.R. Barrett, W.D. Nix, A.S. Tetelman, *The Principles of Engineering Materials* (Prentice, New Jersey, 1973)
25. J.M. Koo, S.B. Jung, Microelectron. Reliab. **47**, 2169 (2007)
26. D. Broek, *Elementary Engineering Fracture Mechanics* (Kluwer, Dordrecht, 1982)
27. D.L. Su, *Mechanical Properties of Engineering Materials* (Mechanical Industry Press, Beijing, 2003)
28. I. Shohji, K. Yasuda, T. Takemoto, Mater. Trans. **46**, 2329 (2005)
29. F.Q. Lang, H. Tanaka, O. Munegata, T. Taguchi, T. Narita, Mater. Charact. **54**, 223 (2005)
30. I. Shohji, T. Yoshida, T. Takahashi, S. Hioki, Mater. Sci. Eng. A. **366**, 50 (2004)
31. H. Rhee, K.N. Subramanian, A. Lee, J.G. Lee, Solder. Surf. Technol. **15**, 21 (2003)
32. H.X. Xie, N. Chawla, Y.L. Shen, Microelectron. Reliab. **51**, 1142 (2011)
33. W.R. Osório, L.C. Peixoto, L.R. Garcia, N. Mangelinck-Noël, A. Garcia, J. Alloys Compd. **572**, 97 (2013)
34. Y.X. Zhu, X.Y. Li, R.T. Gao, C. Wang, J. Mater. Sci. **25**, 3863 (2014)
35. Y.X. Zhu, X.Y. Li, C. Wang, R.T. Gao, J. Mater. Sci. **25**, 1429 (2014)
36. Y.X. Zhu, X.Y. Li, R.T. Gao, C. Wang, Microelectron. Reliab. **54**, 2922 (2014)
37. Q.K. Zhang, Z.F. Zhang, Mater. Sci. Eng. A. **580**, 374 (2013)
38. T.T. Dele-Afolabi, M.A.A. Hanim, M. Norkhairunnisa, H.M. Yusoff, M.T. Suraya, J. Alloys Compd. **649**, 368 (2015)
39. Q.K. Zhang, W.M. Long, X.Q. Yu, Y.Y. Pei, P.X. Qiao, J. Alloys Compd. **622**, 973 (2015)
40. Q.K. Zhang, Z.F. Zhang, Acta. Mater. **59**, 6017 (2011)
41. J. Keller, D. Baither, U. Wilke, G. Schmitz, Acta. Mater. **59**, 2731 (2011)
42. J.H.L. Pang, T.H. Low, B.S. Xiong, L.H. Xu, C.C. Neo, Thin Solid Films **462–463**, 370 (2004)
43. J.G. Maveety, P. Liu, J. Vijayen, F. Hua, E.A. Sanchez, J. Electron. Mater. **33**, 1355 (2004)

44. H.T. Lee, M.H. Chen, H.M. Jao, T.L. Liao, Mater. Sci. Eng. A. **358**, 134 (2003)
45. M. Abtew, G. Selvaduray, Mater. Sci. Eng. R. **27**, 95 (2000)
46. Q.K. Zhang, J. Tan, Z.F. Zhang, J. Appl. Phys. **110**, 014502 (2011)
47. H.C. Cheng, C.F. Yu, W.H. Chen, J. Mater. Sci. **47**, 3103 (2012)

Publisher's Note Springer Nature remains neutral with regard to jurisdictional claims in published maps and institutional affiliations.